Ultramicroscopy 112 (2012) 39–46

Contents lists available at SciVerse ScienceDirect

Ultramicroscopy

journal homepage: www.elsevier.com/locate/ultramic

Optimum HRTEM image contrast at 20 kV and 80 kV—Exemplified by graphene

Z. Lee [a], J.C. Meyer [a,b], H. Rose [a], U. Kaiser [a,*]

[a] Ulm University, Central Facility of Electron Microscopy, Group of Electron Microscopy of Materials Science, Albert Einstein Allee 11, 89081 Ulm, Germany
[b] University of Vienna, Department of Physics, 1090 Vienna, Austria

ARTICLE INFO

Article history:
Received 4 August 2011
Received in revised form
17 October 2011
Accepted 20 October 2011
Available online 30 October 2011

Keywords:
Graphene
Elastic scattering
Phase object approximation
Low voltage
Chromatic aberration

ABSTRACT

The dependence of high-resolution transmission electron microscopy (HRTEM) image contrast of graphene on the adjustable parameters of an aberration-corrected microscope operated at 80 and 20 kV has been calculated and, for 80 kV, compared with measurements. We used density functional theory to determine the projected atom potential and obtained the image intensity by averaging over the energy distribution of the imaging electrons, as derived from the electron energy loss spectroscopy measurements. Optimum image contrast has been determined as a function of energy spread of the imaging electrons and chromatic aberration coefficient, showing that significant improvement of contrast can be achieved at 80 kV with the help of a monochromator, however at 20 kV only with chromatic aberration correction and bright atom contrast conditions.

1. Introduction

With the practical realization of aberration correction [1,2], the old dream of high-resolution imaging of radiation-sensitive organic (low Z-number) structures [3] could soon become reality; thanks to a new generation of low-voltage electron microscopes [4–6]. Recently we first reported experimental findings on spherical aberration-corrected high-resolution transmission electron microscopy (HRTEM) image contrast of graphene and silicon at 20 kV [7]. While these and other recent studies were utilizing hardware correctors only for the geometric aberrations of the TEM objective lens [1,2,8], the next generation of electron microscopes aims for additional chromatic aberration correction, which is mandatory at low voltages [5–7,9]. Within the frame of the Sub-Angstrom Low-Voltage Electron Microscopy (*SALVE*) project our team is currently working on the construction of a microscope that corrects aberrations of the objective lens to such an extent that a resolution of 172 pm at 20 kV will be achieved (this implies that an aperture angle up to 50 mrad can be used [7]). This development has prompted us to review the modeling of the HRTEM image contrast for low voltages.

HRTEM image calculations are conventionally performed by a multi-slice algorithm for modeling the interaction of the electron beam with the sample, a "contrast transfer function" (CTF) to model the geometric aberrations, and envelope functions in order to account for the finite lateral and temporal coherence of the source as well as instabilities [10,11]. To describe non-linear imaging by means of mixed temporal and spatial damping envelope functions, interference of diffracted beams has to be accounted for, and a non-linear transfer function (also called transmission cross-coefficient) has to be applied [12–15]. In addition to this first-order non-linear imaging theory, a full non-linear imaging theory was proposed by Pulvermacher [16], Rose [17], and Bonevich and Marks [18] (for an overview see also [19]). An interesting approach to account for damping effects by averaging the image intensity over the energy distribution of the source electrons has been reported in [20–22]. For an ultra-thin sample, one might be tempted to employ a weak-phase object approximation (WPOA) for the beam-sample interaction and a linear image approximation (including envelopes) to model the effect of the microscope. In the present work, we explore whether these approximations are justified for the case of graphene, which is the thinnest conceivable sample among the currently available materials.

In this paper we report on high-resolution TEM image contrast calculations for imaging with 80 keV and 20 keV electrons following the general approach used in [20–22] but accounting for the effects from energy distribution, broadening, and instabilities using the electron energy loss spectroscopy (EELS) measurements of the elastically scattered imaging electrons. Since we consider a single-atomic-layer sample, the multi-slice simulation is reduced to a single-slice calculation, and the phase shift in the exit wave is

* Corresponding author.
E-mail address: ute.kaiser@uni-ulm.de (U. Kaiser).

0304-3991/$ - see front matter © 2011 Elsevier B.V. All rights reserved.
doi:10.1016/j.ultramic.2011.10.009

proportional to the projected potential (phase object approximation, POA). When no non-linear contributions to the image contrast are present at optimum imaging conditions, positive and negative image contrasts cancel each other [23]; in other words, their difference is a measure for the applicability of the WPOA.

We chose graphene as test object since it is the thinnest possible sample and can be prepared as a clean, free-standing membrane of precisely mono-atomic thickness [24]. Calculations and experiments can thus be compared to each other with much lower uncertainty than for any other TEM specimen. In addition, graphene has a well-known lattice structure [25] and is very stable at electron energies below 80 keV [26]. Moreover, graphene is of great practical interest as it exhibits fascinating physical properties [27]. The recent development of new preparation methods enables production of large area single-layer and bi-layer graphene of high quality [28–31]. Therefore, basic TEM studies of defects in graphene [25,32,33] or atoms on top of graphene [34,35] can now be performed. For a correct evaluation of the experimental contrast of graphene images, it is important to calculate the image contrast based on the appropriate model at the voltage necessary for destruction-free imaging. Although, in general, an 80 keV electron beam should suffice for destruction-free HRTEM imaging of graphene, deviations from the pristine structure and adsorbate atoms on top of graphene can lead to the removal of carbon atoms even at energies below 80 keV [6,36,37]. For example, dangling bond atoms at single vacancies can be displaced at energies ~70 keV and edge atoms even at ~50 keV [38]. Therefore, imaging at lower voltages is desirable.

2. Method

2.1. Calculation procedure

We employ an image calculation procedure that takes into account the finite energy distribution of the imaging electrons by an explicit summation over many images calculated with slightly different energies. Instead of approximating this energy distribution by a Gaussian [20] or Maxwell distribution [22] we normalize the experimentally acquired zero-loss peak extracted from EELS data. This includes the energy distribution of the source and all additional energy broadening effects due to instabilities (since only the zero-loss peak of the EELS spectrum is included we do not account to inelastic scattering).

To find the optimum imaging conditions for graphene, we use an automated search for the highest contrast as a function of defocus and third-order spherical aberration.

Our approach can be divided into four steps (a)–(d):

(a) *Exit wave calculation.*
We calculated the projected atom potential based on DFT calculations [32,39] and the exit wave based on the POA (when using the DFT based potentials, the graphene contrast is ca. 8% reduced compared to the independent atom model).

(b) *Normalization of the zero-loss peak (determination of the weighting factor $D(\Delta E)$).*
After the electrons have transmitted the object their energy distribution has been changed by inelastic scattering, which can be measured from the corresponding EELS data. As we use an energy filter for HRTEM imaging, the inelastic scattered electrons are removed and do not contribute to the image contrast. Therefore we only need to consider in the EELS spectra the area under the zero-loss peak $|(\Delta E|_{max} = 2\,\mathrm{eV})$. The normalized EELS data provides a weighting function $D(\Delta E)$. This function includes all contributions to the energy spread of the primary beam.
For each energy deviation $\Delta E = E - E_0$ from the mean electron energy E_0, we calculate the corresponding image wave $\psi_i(\Delta E)$ based on the convolution of the exit wave ψ_e and the transfer function $\exp(i\chi)$ (see [20]), where the wave aberration phase factor $\chi = \chi_g + \chi_c$ depends on the spatial frequency q and is composed of the geometric phase χ_g:

$$\chi_g = \pi(0.5 C_s \lambda^3 q^4 + \Delta f \lambda q^2), \tag{1}$$

and the chromatic phase χ_c:

$$\chi_c = \frac{\pi C_c \lambda q^2 \Delta E}{E_0}, \tag{2}$$

where λ—the wave length; C_s—the spherical aberration coefficient; C_c—the chromatic aberration coefficient; Δf—the defocus.

(c) *Determination of the total image intensity.*
In our approach, the total image intensity is then determined by

$$I = \int \psi_i \psi_i^* D(\Delta E) d(\Delta E), \tag{3}$$

which is the summation of all intensities $\psi_i(\Delta E)\psi_i^*(\Delta E)$, multiplied by the weighting factor $D(\Delta E)$ obtained from the normalized zero loss EELS peak.

(d) *Determination of optimum imaging conditions.*
For a non-corrected TEM with fixed C_s, the optimum imaging condition is estimated through optimizing the phase contrast transfer function (PCTF) by adjusting Δf appropriately [40,41]. In the case of a C_s-corrected TEM, the optimum values for Δf and C_s depend on the information limit q_l of the microscope [42,43].

In our image calculation and in the experiments, we have evaluated the atom contrast after Watson et al. [44]. In order to make the sign consistent with the definition of Zernike [45], where the atom appears darker than the background for positive contrast (dark atom contrast), and brighter for negative contrast (bright atom contrast), we write for the atom contrast C_a:

$$C_a = \frac{I_b - I_a}{I_b}, \tag{4}$$

where I_a is the image intensity at the center of the atom, and I_b is the intensity at the center of the background (for graphene: center of the hexagon). A universal criteria for minimizing delocalization and optimizing phase contrast over a broad range of spatial frequencies is suggested by Lentzen as $\int |\chi_g(q) - \chi_0|^2 dq \rightarrow \min$ [43], where χ_0 is the ideal constant phase shift. This least-square fit method aims to find the highest-contrast imaging condition for the needed range of spatial frequencies.

In our case, as only one defined spatial frequency is needed to construct the graphene lattice ($4.69\ \mathrm{nm}^{-1}$), the information transfer does not need to be maximized for a range of spatial frequencies. We calculate the image intensity for series of (C_s, Δf) pairs (Eq. (3)) and determine the corresponding contrast (Eq. (4)). The (C_s, Δf) pair, producing maximum (optimum) contrast, is finally selected.

2.2. Computational and experimental details

The scripts for image calculation were written in Matlab R2009b (The Mathworks Inc.). To elucidate the imaging parameters that provide optimum imaging conditions for graphene, we have varied C_s and Δf for acceleration voltages of 80 and 20 kV, respectively. The optimum imaging parameters were determined from the maximum atom contrast. For the calculations at 20 kV,

we model a Libra microscope equipped with a C_s corrector. The chromatic aberration coefficient for this microscope is C_c= 1.41 mm at 80 kV and C_c=1.26 mm at 20 kV [7]. The image calculation was performed in four steps: (1) Calculation of exit wave using the projected atom potential. (2) Setting the range for variation of the free aberration parameters C_s and Δf to $-100\ \mu m \le C_s \le 100\ \mu m$ and $-30\ nm \le \Delta f \le 30\ nm$, respectively, with an increment of 0.5 μm for C_s and 0.2 nm for Δf. (3) Normalization of area below the zero loss EELS peak by $\int D(\Delta E)d(\Delta E)=1$. The step size of ΔE (0.019 eV) equals the sampling rate of the EELS data. (4) Determination of image intensity for each (C_s,Δf) pair located within the parameter range defined in (2).

Single-layer graphene samples were prepared by mechanical cleaving and transferred to TEM grids as described previously [46]. Electron energy loss spectra (EELS) were recorded from single-layer graphene regions. HRTEM imaging has been performed using a FEI Titan 80–300. The extraction voltage of the source was lowered to 2 kV. This measure reduced the energy spread from 0.6 to ~0.4 eV [47]. EELS data was recorded on a Tridiem GIF spectrometer. The spherical aberration was adjusted close to zero (0 ± 4 μm).

HRTEM images at 80 kV were recorded on the GIF camera (Gatan model US1000) with 2048×2048 pixels. Due to the 20× post-magnification of the GIF camera, extremely high spatial sampling of 40 pixels per Angstrom was achieved for a small region of the sample. In this way, we minimized effects of camera modulation transfer [48]. We recorded focal series of single-layer graphene and measured the contrast for each defocus value averaging over the visible unit cells in the contamination-free area.

For the 20 kV case, EELS spectra were recorded using a monochromated Zeiss Libra 200 equipped with an in-column energy filter. Although we obtained experimental images of graphene at 20 kV [7], these were not analyzed due to incomplete compensation of geometric aberrations in this preliminary experimental setup.

3. Image contrast based on WPOA

To understand the differences of image contrast based on POA and WPOA, we present a short review of WPOA. Phase objects are generally considered to be very thin and to change the phase of the incident wave only up to the exit plane z_e [20]. The resulting exit wave $\psi_e(\vec{\rho})$is given by

$$\psi_e(\vec{\rho}) = e^{i\sigma V_p(\vec{\rho})}, \quad V_p(\vec{\rho}) = \int_{-\infty}^{\infty} V(\vec{r})dz, \tag{5}$$

σ is the interaction parameter measuring the extent of electron scattering by the sample, given by $\sigma=(\pi/\lambda E)$ (λ—wave length; E—accelerating voltage). The projected atom potential $V_p(\vec{\rho})$ is taken in the propagation direction of the incident plane wave. Here we have assumed that the illumination is parallel to the optic axis, which we choose as the z-axis of our Cartesian coordinate system. If the exponent $\sigma V_p(\vec{\rho})$ is small compared to unity, we can expand the exit wave in a Taylor series. The first two terms $1+i\sigma V_p(\vec{\rho})$ give the so-called weak phase object approximation (WPOA). For centrosymmetic crystals (as is the case for graphene) we have $V(\vec{q}) = V^*(-\vec{q})$. As seen from Eqs. (1) and (2), $\chi(\vec{q}) = \chi(-\vec{q})$and the resulting image intensity has the standard form:

$$I = \int I_{\Delta E}(r)D(\Delta E)d(\Delta E)$$
$$= 1-2\sigma \int FT^{-1}[A(q)V(q)\sin\chi]D(\Delta E)d(\Delta E). \tag{6}$$

The first term in the second row describes the background intensity. The second term defines the phase contrast. The aperture function $A(q)$ treats the effect of a beam-limiting aperture placed at the back-focal plane of the objective lens. The weighting function $D(\Delta E)$ describes the energy spread of the scattered electrons. After correcting the chromatic aberration (χ_c=0), the phase $\chi=\chi_g$ reverses its sign when the signs of C_s and Δf are interchanged (see Eq. (1)). In this case, the image contrast described by Eq. (4) changes its sign but not its absolute value.

4. Results and discussion

4.1. Optimum imaging conditions for graphene with and without chromatic aberration

Calculated images of graphene for 80 kV utilizing the EELS data are shown in Fig. 1 for C_s and Δf in the ranges of $-100\ \mu m \le C_s \le 100\ \mu m$ and $-30\ nm \le \Delta f \le 30\ nm$, respectively (see Eq. (3)). Interestingly, the images look very similar for a wide range of (C_s, Δf) values. Three diagonals of equal contrast (within the error margin ±0.1%) for bright and dark atom contrasts, respectively, are marked. As can be seen, the highest dark and bright atom contrasts are obtained along the middle marked diagonals. We select the two images marked by the red rectangles as representative examples (located in the center of the highest-contrast diagonal). Fig. 2a presents calculated images of graphene. The two chosen images from Fig. 1 are depicted in the right column. The achromatic images (χ_c=0) shown in the left column of Fig. 2a are selected by following the same approach. Fig. 2b shows the experimental images (see Section 4.3 for more details). By taking into account the chromatic aberration error of the objective lens, the calculated optimum contrast (Fig. 2a, right column) quantitatively (within the error margins) matches the experimental image contrast (Fig. 2b). In our case there is no Stobbs factor between experimental and calculated images within the error margin; the influence of the MTF is avoided owing to the extremely high sampling rate, see Section 4.3. Moreover, the image contrast also compares reasonably well to calculations using the conventional temporal envelope approach (focal spread of 40 Å for 80 kV) (~9.0% for both the optimum negative and positive contrast, not shown). This result agrees with earlier works on positive and negative contrast, which show that at medium voltages, the sum of the contrasts largely cancel out for ultra-thin samples [49].

At 20 kV (see Fig. 3), the measured energy distribution shows a FWHM of 0.12 eV obtained with the help of monochromator. Experimental images with atomic resolution are not available for comparison because our present corrector can only compensate for geometric aberrations up to 25 mrad (40 mrad would be required for graphene at 20 kV). Without chromatic aberration correction (compare Fig. 2a, right column and Fig. 3, right column), the absolute values of optimum positive and optimum negative contrast at 20 kV are not significantly higher than at 80 kV. Strong differences arise only when eliminating chromatic aberration by means of a C_c-corrector (C_c=0) or an ideal monochromator (E_w=0). Since an ideal monochromator removes an intolerably large fraction of electrons, a significant increase in contrast at low voltages necessitates correction of chromatic aberration.

The achromatic image calculations show symmetric (C_s/Δf) values for optimum negative and positive atom contrast for both, 80 and 20 kV (see Figs. 1a and 2 left images). However, the respective absolute contrast values differ considerably. This is a fingerprint of the contrast contributions from non-linear terms. The absolute contrast difference increases as the voltage decreases. As mentioned above, in order to treat an object as an ideal WPO, the absolute values of optimum positive and optimum negative contrast must be roughly equal for achromatic imaging

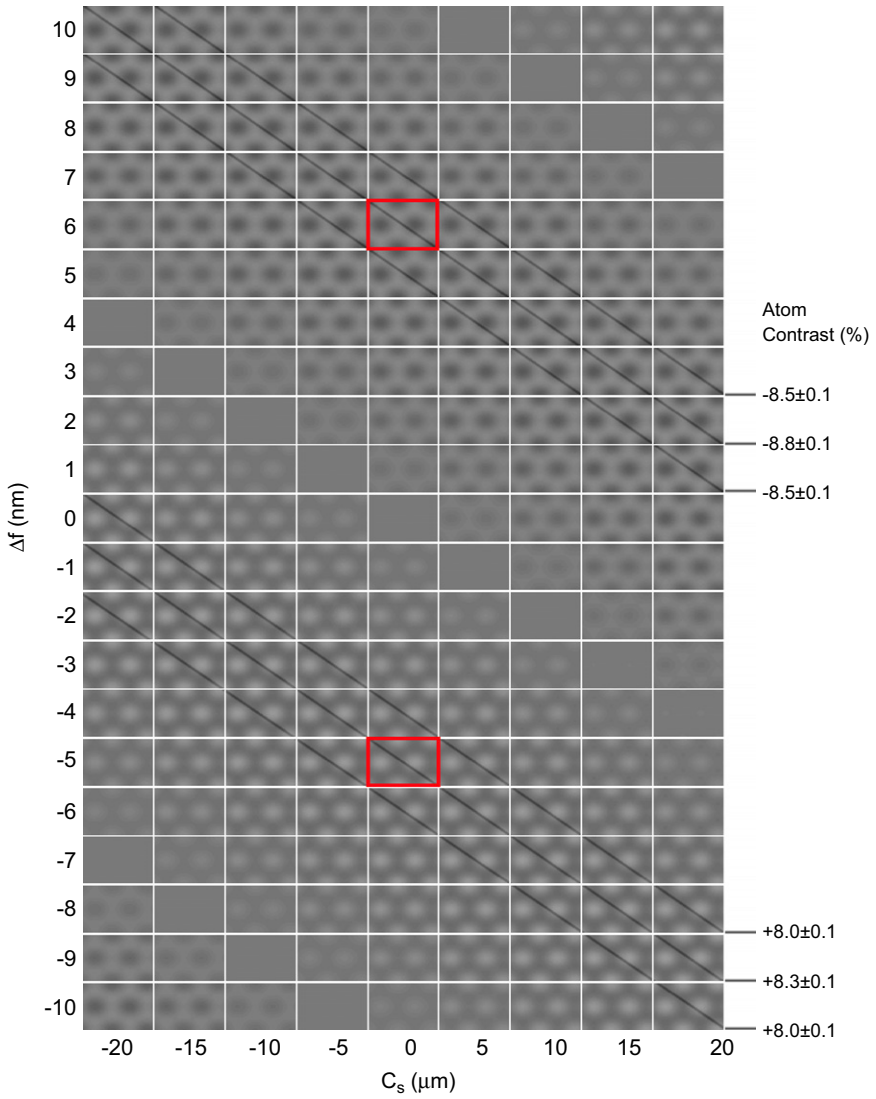

Fig. 1. C_s–Δf table ($-100\ \mu m \le C_s \le 100\ \mu m$, $-30\ nm \le \Delta f \le 30\ nm$) for the calculated HRTEM images of graphene at 80 kV, with $C_c = 1.41$ mm, and energy distribution extracted from the EELS data. The highest dark and bright atom contrasts are obtained for a set of C_s–Δf values marked by the middle diagonals. The two images marked by the red rectangles are in the center of the highest-contrast diagonal representing optimum contrast values. (For interpretation of the references to color in this figure legend, the reader is referred to the web version of this article.)

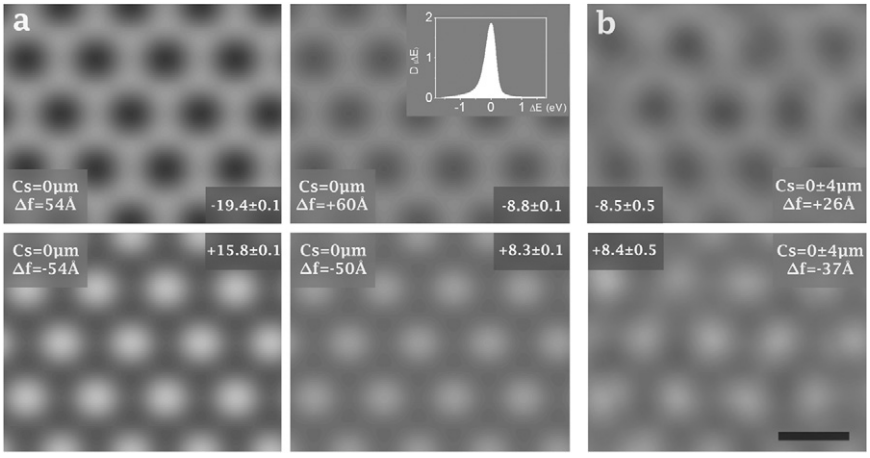

Fig. 2. HRTEM images of graphene at 80 kV for optimum contrast conditions showing negative (upper row) and positive (lower row) carbon atom contrast. The optimum (C_s, Δf) values and corresponding maximum contrast (multiplied by 100) are given in the images. (a) Calculated images for $C_c = 0$ (first column) and for $C_c = 1.41$ mm with energy distribution acquired from normalized experimental zero loss peak (second column). The inset depicts the EELS spectra of the zero-loss peak with energy width of $E_w = 0.35$ eV. (b) Experimental images. The error bars in the calculated and experimental images result from the fluctuations of background and atom intensities. Scale bar: 0.2 nm.

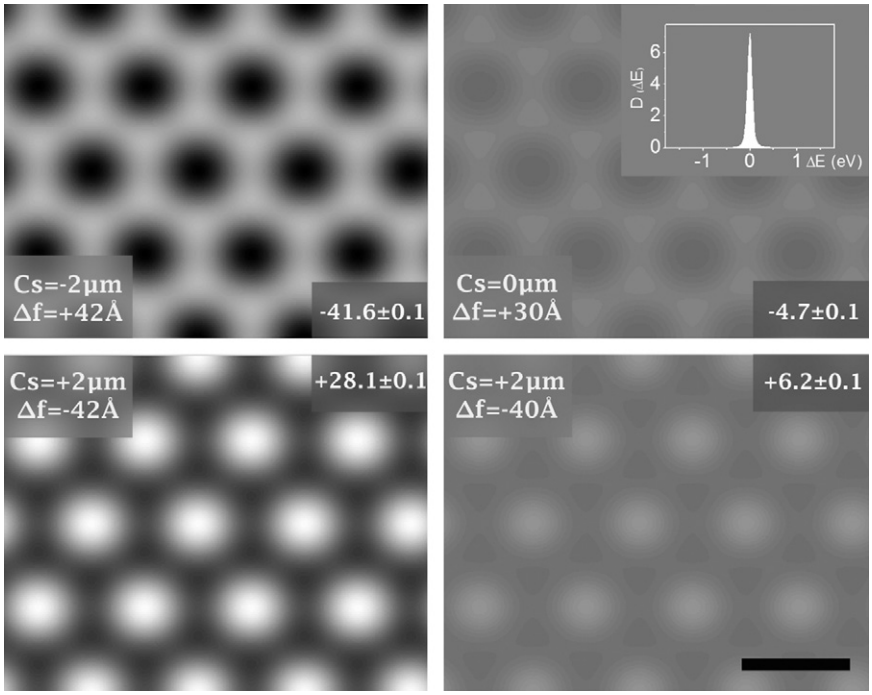

Fig. 3. HRTEM images of graphene at 20 kV for optimum contrast conditions showing negative (upper row) and positive (lower row) carbon atom contrast. Parameters: left column: $C_c=0$ (or an ideal monochromatic electron beam $E_w=0$). Right column: $C_c=1.26$ mm, $E_w=0.12$ eV (from inset, the experimental EELS spectra of the zero-loss peak). The error bars in the calculated image results from the fluctuation of background and atom intensity. Scale bar: 0.2 nm.

conditions. When going from 80 to 20 kV, the contribution of non-linear terms to the image contrast can no longer be ignored since the interaction parameter σ increases with decreasing voltage (this means the second line of Eq. (6) is incomplete). Hence at 20 kV, even light atoms such as carbon are strong electron scatters. Moreover, there may be significant contributions due to inelastic scattering at 20 kV, which are not considered in the present work. As we neglect inelastic scattering in our calculations, we consequently also neglect the phonon scattering.

The achromatic bright atom contrast image in Fig. 3 (20 kV) demonstrates two very strong contrast enhancement effects: first the advantage of chromatic aberration correction (compare the achromatic and chromatic images), and second the advantage of bright atom contrast imaging (compare the images in the first column). The effect of bright atom contrast enhancement has already been mentioned in [49,50]. At 20 kV, even for a highly monochromatic electron source, resulting in a small E_w of 0.12 eV, the contrast values differ by a factor >8 (<5) for bright (dark) atom contrast, compared to the cases without chromatic corrections. Hence the correction of chromatic aberration and bright atom contrast imaging conditions are indispensable for achieving high contrast at voltages as low as 20 kV.

4.2. Evaluation of contrast dependence on chromatic aberration and energy width

In the following we investigate the dependence of the optimum atom contrast on chromatic aberration (Fig. 4a) and energy width (Fig. 4b) in more detail. Fig. 4 shows that the absolute optimum atom contrast at 20 kV decreases strongly with increasing C_c (Fig. 4a, red curves) and E_w (Fig. 4b, red curves), much stronger than that at 80 kV (Fig. 4a and b, blue curves). At 20 kV, bright and dark atom contrasts (light and dark colors, respectively) have large values for the achromatic case ($C_c=0$, $E_w=0$). Without chromatic aberration, the constructive superposition of linear and non-linear terms results in enhanced contrast (bright atom contrast) [49], while the destructive superposition results in reduced contrast (dark atom contrast). With increasing chromatic aberration, bright atom contrast decreases stronger than dark atom contrast. As a result, both curves intersect each other, as shown in Fig. 4a. At 80 kV, a contrast increase of about a factor of 2 (from about 8% to 16%) can be achieved with a monochromator, which reduces the energy width from $E_w\sim0.35$ to 0.12 eV (as marked by the corresponding dashed lines in Fig. 4b). Compared to this case, the use of a C_c correction provides only little contrast increase (from about 16% to 19%). However, this behavior does not hold true in the case of 20 kV. Fig. 4b shows that for 20 kV, the contrast drops to about zero in presence of chromatic aberration for energy widths larger than about 0.2 eV. For the achromatic case, the absolute values of bright and dark atom contrast and their differences are much larger at 20 kV than at 80 kV. At 20 kV, even the use of an effective monochromator (0.12 eV energy width) is not sufficient because the resulting optimum contrast values are rather small (about 6% and 5% for dark and bright atom contrast, respectively, see also the images in Fig. 3, right column). However, the addition of C_c correction tremendously increases the contrast in 20 kV TEM images. Hence, one of the key promises of low-voltage microscopy – high contrast for low-Z materials – can only be achieved with the use of a C_c corrector.

4.3. Experimental image contrast at 80 kV

In order to find the maximum contrast for single-layer graphene, we analyze a closely spaced focal series (defocus step size 0.53 nm) with spherical aberration close to zero giving symmetric conditions for positive and negative defocus. Several experimental images are shown in Fig. 5, together with the measured contrast vs. defocus plot. Note that the images measures only about 20 unit cells in diameter but were recorded with the full 2048×2048 pixels resolution of the CCD camera. Due to this extremely high oversampling (40 pixels per Angstrom), we obtain

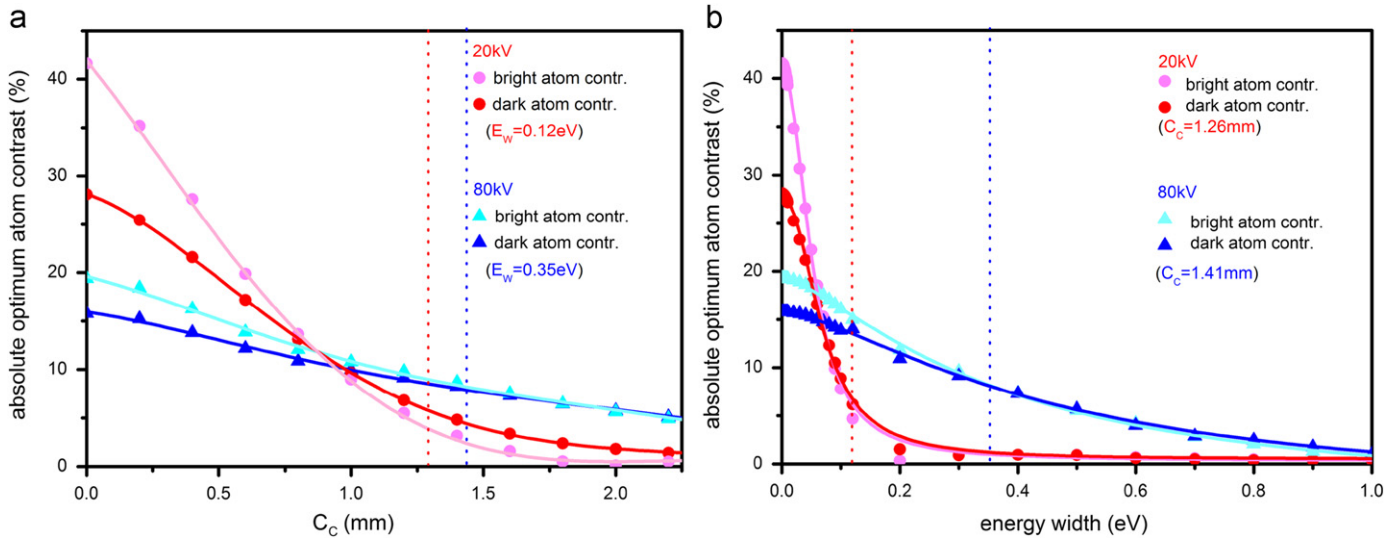

Fig. 4. (a) Calculated absolute optimum atom contrast of graphene (a) as a function of the chromatic aberration coefficient C_c and (b) as a function of the energy width (E_w) of the zero loss peak for 20 kV (red circle) and 80 kV (blue triangle) for bright (light color) and dark (strong color) atom contrasts. The corresponding experimental parameters for C_c and E_w are indicated in the figures by the dashed lines. The variable energy width in (b) is obtained by proportionally shrinking or stretching the zero-loss peak extracted from the experimental EELS data. (For interpretation of the references to color in this figure legend, the reader is referred to the web version of this article.)

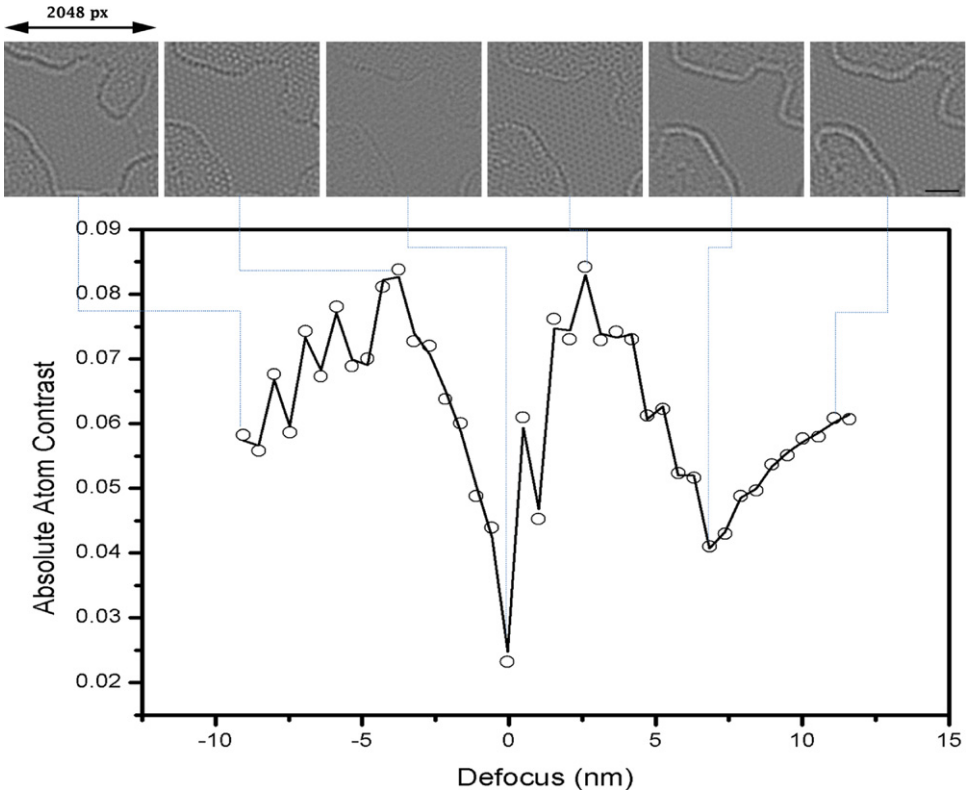

Fig. 5. Absolute atom contrast at 80 kV and $C_s \sim 0$ μm for single-layer graphene as a function of defocus. As predicted by calculation, the maximum contrasts for bright atom and dark atom conditions are nearly identical. Scale bar: 1 nm.

8–9% contrast for single-layer graphene (At a more common sampling of ~5 pixel per angstrom, the contrast is ca. 2× smaller; in agreement with a measured camera MTF [48]). In the experimental contrast vs. defocus plot, all contrast values are given as positive numbers because the sign is difficult to determine close to the minima. In any case, the "negative" (bright atom) contrast is present from roughly 0 to 7 nm defocus. Zero defocus is assigned at the contrast minimum where also the contamination contrast vanishes.

In the experimental curve, we find a maximum contrast of 8.5% for bright-atom condition (defocus +2.6 nm) and 8.4% for the dark-atom maximum (defocus −3.7 nm). The contrast values are approximately identical, as predicted by our calculations. Hence, the experimental result confirms that graphene can be

treated at 80 kV as weak phase object with a sufficient degree of accuracy.

5. Conclusion

For 80 and 20 kV we have calculated optimum C_s-corrected HRTEM image contrast, based on the criteria for maximum atom contrast. We exemplified this criterion by graphene. We used DFT-based projected atom potential and calculated, for the first time, the image intensity by averaging over the energy distribution of the elastically scattered imaging electrons, derived from the experimental EELS data. At 80 kV, this approach agrees quantitatively with the conventional envelope method and the experimental data. Neither a Stobbs factor nor a difference between bright and dark atom contrasts was measured within our measurement accuracy under the given experimental conditions. We demonstrated that at 80 kV the image contrast can be increased effectively by a monochromator capable of reducing the energy width to about 0.1 eV.

At 20 kV, atomically resolved images cannot be experimentally obtained owing to incomplete compensation of geometric aberrations in our preliminary experimental setup. Significant improvement of contrast can only be achieved by the additional correction of chromatic aberration. Moreover, we show that a further increase of contrast is possible using bright atom imaging conditions, even for a single layer of atoms. Our calculations clearly show that even graphene cannot be treated as a weak phase object. In other words, all atoms are strong scatters at voltages smaller than about 20 kV.

Acknowledgment

We thank Lorenz Lechner for the fruitful discussions and Simon Kurasch for the DFT based potential calculation of graphene. We gratefully acknowledge financial support by the German Research Foundation (DFG) and the Ministry of Science, Research, and Arts (MWK) of the state Baden Württemberg within the Sub-Angstrom Low-Voltage Electron Microscopy (SALVE) Project as well as by the DFG within the SFB 569.

References

[1] H. Rose, Outline of a spherically corrected semi-aplanatic medium-voltage TEM, Optik 85 (1990) 19–24.
[2] M. Haider, H. Rose, S. Uhlemann, B. Kabius, K. Urban, Towards 0.1 nm resolution with the first spherically corrected transmission electron microscope, Journal of Electron Microscopy 47 (5) (1998) 395–405.
[3] M. Segal, Surely you're happy, Mr. Feynman! Nature Nanotechnology 4 (2009) 786–788.
[4] H. Rose, Future trends in aberration-corrected electron microscopy, Philosophical Transactions of the Royal Society A 367 (2009) 3809–3823.
[5] H. Sawada, T. Sasaki, F. Hosokawa, S. Yuasa, M. Terao, M. Kawazoe, T. Nakamichi, T. Kaneyama, Y. Kondo, K. Kimoto, K. Suenaga, Higher-order aberration corrector for an image-forming system in a transmission electron microscope, Ultramicroscopy 110 (2010) 958–961.
[6] U. Kaiser, A. Chuvilin, J.C. Meyer, J. Biskupek, Microscopy at the bottom. In: W. Grogger, F. Hofer, P. Poelt (Eds.), Materials Science Microscopy Conference MC2009, vol. 3, 2009, pp. 1–6.
[7] U. Kaiser, J. Biskupek, J.C. Meyer, J. Leschner, L. Lechner, H. Rose, M. Stöger-Pollach, A.N. Khlobystov, P. Hartel, H. Müller, M. Haider, S. Eyhusen, G. Benner, Transmission electron microscopy at 20 kV for imaging and spectroscopy, Ultramicroscopy 111 (2011) 1239–1246.
[8] M. Haider, S. Uhlemann, E. Schwan, H. Rose, B. Kabius, K. Urban, Electron microscopy image enhanced, Nature 392 (1998) 768–769.
[9] M. Haider, H. Müller, S. Uhlemann, J. Zach, U. Loebau, R. Hoeschen, Prerequisites for a C_c/C_s-corrected ultrahigh-resolution TEM, Ultramicroscopy 108 (2008) 167–178.
[10] J. Frank, The envelope of electron microscopic transfer functions for partially coherent illumination, Optik 38 (1973) 519.
[11] W.O. Saxton, Spatial coherence in axial high resolution conventional electron microscopy, Optik 49 (1977) 51.
[12] R.H. Wade, J. Frank, Electron microscope transfer functions for partially coherent axial illumination and chromatic defocus spread, Optik 49 (1977) 81.
[13] K. Ishizuka, Contrast transfer of crystal images in TEM, Ultramicroscopy 5 (1980) 55–65.
[14] E.J. Kirkland, Nonlinear high resolution image processing of conventional transmission electron micrographs: I. Theory, Ultramicroscopy 9 (1982) 45–64.
[15] W.M.J. Coene, A. Thust, M. Op de Beeck, D. Van Dyck, Maximum-likelihood method for focus-variation image reconstruction in high resolution transmission electron microscopy, Ultramicroscopy 64 (1996) 109–135.
[16] H. Pulvermacher, Transmission cross-coefficient for electron microscopic imaging with partially coherent illumination and electric instability, Optik 60 (1981) 45.
[17] H. Rose, Information transfer in transmission electron microcopy, Ultramicroscopy 15 (1984) 173–191.
[18] J.E. Bonevich, L.D. Marks, Contrast transfer theory for non-linear imaging, Ultramicroscopy 26 (1988) 313–319.
[19] R. Erni, Aberration-Corrected Imaging in Transmission Electron Microscopy: An Introduction, Imperial College Pr., 2010.
[20] L. Reimer, H. Kohl, Transmission Electron Microscopy: Physics of Imaging Formation, Springer, 2008.
[21] E.J. Kirkland, Advanced Computing Electron Microscopy, Plenum Press, 1998.
[22] H. Rose, Theoretical aspects of image formation in the aberration-corrected electron microscope, Ultramicroscopy 110 (2010) 488–499.
[23] Z.L. Zhang, U. Kaiser, Structural imaging of β-Si_3N_4 by spherical aberration-corrected high-resolution transmission electron microscopy, Ultramicroscopy 109 (2009) 1114–1120.
[24] J.C. Meyer, A.K. Geim, M.I. Katsnelson, K.S. Novoselov, T.J. Booth, S. Roth, The structure of suspended graphene sheets, Nature 446 (2007) 60.
[25] J.C. Meyer, C. Kisielowski, R. Erni, M.D. Rossell, M.F. Crommie, A. Zettl, Direct imaging of lattice atoms and topological defects in graphene membranes, Nano Letters 8 (2008) 3582–3586.
[26] J.C. Meyer, A. Chuvilin, U. Kaiser, Graphene—two-dimensional carbon at atomic resolution in MC2009, in: W. Grogger, F. Hofer, P. Polt (Eds.), Materials Science, vol. 3, Graz, 2009, pp. 347–348.
[27] A.K. Geim, K.S. Novoselov, The rise of graphene, Nature Materials 6 (2007) 183–191.
[28] T.J. Booth, P. Blake, R.R. Nair, D. Jiang, E.W. Hill, U. Bangert, A. Bleloch, M. Gass, K.S. Novoselov, M.I. Katsnelson, A.K. Geim, Macroscopic graphene membranes and their extraordinary stiffness, Nano Letters 8 (2008) 2442–2446.
[29] A.N. Obraztsov, E.A. Obraztsova, A.V. Tyurnina, A.A. Zolotukhin, Chemical vapor deposition of thin graphite films of nanometer thickness, Carbon 45 (2007) 2017–2021.
[30] H.J. Park, J. Meyer, S. Roth, V. Skákalová, Growth and properties of few-layer graphene prepared by chemical vapor deposition, Carbon 48 (2010) 1088–1094.
[31] H.J. Park, V. Skákalová, D.S. Lee, C. Bumby, T. Iwasaki, J. Meyer, U. Kaiser, S. Roth., Growth and properties of chemically modified graphene, Physica Status Solidi B 247 (11–12) (2010) 2915–2919.
[32] J.C. Meyer, S. Kurasch, H.J. Park, V. Skakalova, D. Künzel, A. Groß, A. Chuvilin, G. Algara-Siller, S. Roth, T. Iwasaki, U. Starke, J. Smet, U. Kaiser, Experimental analysis of charge redistribution due to chemical bonding by high-resolution transmission electron microscopy, Nature Materials 10 (2010) 209–215.
[33] J. Kotakoski, A.V. Krasheninnikov, U. Kaiser, J.C. Meyer., From point defects in graphene to two-dimensional amorphous carbon, Physical Review Letters 106 (2011) 105505.
[34] F. Schedin, A.K. Geim, S.V. Morozov, E.W. Hill, P. Blake, M.I. Katsnelson, K.S. Novoselov, Detection of individual gas molecules adsorbed on graphene, Nature Materials 6 (2007) 652–655.
[35] R. Erni, M.D. Rossell, M.-T. Nguyen, S. Blankenburg, D. Passerone, P. Hartel, N. Alem, K. Erickson, W. Gannett, A. Zettl, Stability and dynamics of small molecules trapped on graphene, Physical Review B 82 (2010) 165443.
[36] A. Chuvilin, J. Meyer, G. Algara-Siller, U. Kaiser, From graphene constrictions to single carbon chains, New Journal of Physics 11 (2009) 083019.
[37] Ç.Ö. Girit, J.C. Meyer, R. Erni, Marta D. Rossell, C. Kisielowski, L. Yang, M.F. Crommie, M.L. Cohen, S.G. Louie, A. Zettl, Graphene at the edge: stability and dynamics, Science 323 (2009) 1705–1708.
[38] J. Kotakoski, Private Communication.
[39] S. Kurasch, Graphene Imaging and Chemistry, Diplomarbeit, Universität Ulm, 2009.
[40] O. Scherzer., The theoretical resolution limit of the electron microscope, Journal of Applied Physics 20 (1949) 20.
[41] H. Lichte, Optimum focus for taking electron holograms, Ultramicroscopy 38 (1991) 13–22.
[42] M. Lentzen, B. Jahnen, C.L. Jia, A. Thust, K. Tillmann, K. Urban, High-resolution imaging with an aberration-corrected transmission electron microscope, Ultramicroscopy 92 (2002) 233–242.
[43] M. Lentzen, The tuning of a Zernike phase plate with defocus and variable spherical aberration and its use in HRTEM imaging, Ultramicroscopy 99 (2004) 211–220.
[44] A.B. Watson, H.B. Barlow, J.G. Robson, What does the eye see best? Nature 302 (1983) 412–422.
[45] F. Zernike, Phase contrast, a new method for the microscopic observation of transparent objects part I, Physica 9 (1942) 686–698.

[46] J.C. Meyer, C.O. Girit, M.F. Crommie, A. Zettl, Hydrocarbon lithography on graphene membranes, Applied Physics Letters 92 (2008) 123110.
[47] J.C. Meyer, A. Chuvilin, G. Algara-Siller, J. Biskupek, U. Kaiser, Selective sputtering and atomic resolution imaging of atomically thin boron nitride membranes, Nano Letters 9 (7) (2009) 2683–2689.
[48] A. Thust, High-resolution transmission electron microscopy on an absolute contrast scale, Physical Review Letters 102 (2009) 220810.
[49] C.L. Jia, L. Houben, A. Thust, J. Barthel, On the benefit of the negative-spherical-aberration imaging technique for quantitative HRTEM, Ultramicroscopy 110 (2010) 500.
[50] C.L. Jia, M. Lentzen, K. Urban, High-resolution transmission electron microscopy using negative spherical aberration, Microscopy and Microanalysis 10 (2004) 174–184.